#### **PAPER**

Sb nanocrystal-anchored hollow carbon microspheres for high-capacity and high-cycling performance lithium-ion batteries

To cite this article: Meiqing Guo et al 2020 Nanotechnology 31 135404

View the article online for updates and enhancements.



# IOP ebooks™

Bringing together innovative digital publishing with leading authors from the global scientific community.

Start exploring the collection-download the first chapter of every title for free.

Nanotechnology

Nanotechnology 31 (2020) 135404 (13pp)

# Sb nanocrystal-anchored hollow carbon microspheres for high-capacity and high-cycling performance lithium-ion batteries

Meiqing Guo<sup>1,2,3,4</sup>, Jiajun Chen<sup>1,2</sup>, Weijia Meng<sup>1,2</sup>, Liyu Cheng<sup>1,2</sup>, Zhongchao Bai<sup>5</sup>, Zhihua Wang<sup>1,2,3,6</sup> and Fuqian Yang<sup>4,6</sup>

E-mail: wangzh@tyut.edu.cn and fyang2@uky.edu

Received 19 July 2019, revised 11 November 2019 Accepted for publication 2 December 2019 Published 14 January 2020



#### **Abstract**

There is a great need to develop sustainable and clean energy storage devices and systems of high-energy and high-capacity densities. In this work, we synthesize antimony (Sb) nanocrystal-anchored hollow carbon microspheres (Sb@HCMs) via the calcination of cultivated yeast cells and the reduction of SbCl<sub>3</sub> in an ethylene glycol solution on the surface of hollow carbon microspheres. The Sb@HCMs possess hollow and porous structure, and the Sb is present in the form of nanocrystals. Using the Sb@HCMs as the active-electrode material, we assemble lithium (Li)-ion half cells and full cells and investigate their electrochemical performance. The Li-ion half cells possess a charge capacity of 605 mA h g<sup>-1</sup> after 100 cycles at a current density of 100 mA g<sup>-1</sup> and a charge capacity of 469.9 mA h g<sup>-1</sup> at a current density up to 1600 mA g<sup>-1</sup>, which is much higher than the theoretical capacity of 372 mA h g<sup>-1</sup> for commercial graphite electrode. The Li-ion full cells with Sb@HCMs//LiCoO<sub>2</sub> deliver a charge capacity of 300 mA h g<sup>-1</sup> at a current density of 0.2 A g<sup>-1</sup> after 50 cycles, and have potential in applications of energy storage.

Supplementary material for this article is available online

Keywords: Sb nanocrystals, hollow carbon microspheres, lithium-ion battery, anode

(Some figures may appear in colour only in the online journal)

# 1. Introduction

The use of non-renewable fossil fuels, such as coal, oil and natural gas, has caused severe environmental pollution and climate change, and the rapid consumption of non-renewable fossil fuels has led to a global energy crisis. There is a great need to develop sustainable and clean energy storage devices and systems to address the environmental pollution from the use of non-renewable fossil fuels and the depletion of the non-renewable energy sources.

A variety of devices and systems for energy storage have been developed, including Ag–Zn batteries, lead acid

<sup>&</sup>lt;sup>1</sup> Institute of Applied Mechanics, College of Mechanical and Vehicle Engineering, Taiyuan University of Technology, Taiyuan 030024, People's Republic of China

<sup>&</sup>lt;sup>2</sup> Shanxi Key Laboratory of Material Strength and Structural Impact, College of Mechanical and Vehicle Engineering, Taiyuan University of Technology, Taiyuan 030024, People's Republic of China

<sup>&</sup>lt;sup>3</sup> National Demonstration Center for Experimental Mechanics Education, Taiyuan University of Technology, Taiyuan 030024, People's Republic of China

<sup>&</sup>lt;sup>4</sup> Materials Program, Department of Chemical and Materials Engineering, University of Kentucky, Lexington 40506, United States of America

<sup>&</sup>lt;sup>5</sup> College of Materials Science and Engineering, Taiyuan University of Technology, Taiyuan 030024, People's Republic of China

<sup>&</sup>lt;sup>6</sup> Authors to whom any correspondence should be addressed.

batteries, fuel cells, rechargeable lithium-ion batteries (LIBs) and sodium-ion batteries [1]. Among these devices and systems, LIBs have been deemed as promising clean energy devices and systems and have been widely used in a variety of portable electronic devices, such as cellular phones, digital cameras, laptops, etc, due to their unique electrochemical properties of large energy density, high operation voltage, extended cycle life and environmental friendliness [2-4]. With the potential applications of LIBs in electric vehicles and hybrid photovoltaic-battery systems [5], which require the storage of large-scale energy, there is an increased demand to produce LIBs with high-energy and high-capacity densities [6-8]. Currently, the anode materials used in commercial LIBs are based on graphite, which has a theoretical capacity of only 372 mA h g<sup>-1</sup>, and C-based LIBs cannot meet the requirements of electric vehicles [9]. Also, there exist environmental issues in the fabrication of commercial graphite anodes. Thus, exploiting alternative anode materials with high-energy densities and long-electrochemical cycle life from environmentally-friendly and renewable sources is of practical importance for the applications of LIBs.

There are studies focusing on the use of metallic materials, such as tin (Sn) [10], antimony (Sb) [11] and germanium (Ge) [12], metal oxides, such as SnO<sub>2</sub> [13], TiO<sub>2</sub> [14], Mn<sub>3</sub>O<sub>4</sub> and ZnMn<sub>2</sub>O<sub>4</sub> [2], and graphene-based materials [15], as anode materials in LIBs due to the high theoretical capacities of these materials. Among these metallic materials, Sb with flat potential profile and high theoretical capacity has potential as anode material of LIBs [16]. In addition, the positive intercalation voltage of the Sb-based anode, which is slightly larger than that of Li, can limit the formation of Li dendrites during fast recharging and improve the operational safety of LIBs [17]. However, the large change in specific volume  $(\sim 150\%)$  of Sb due to lithiation/delitation can lead to the pulverization of Sb and local exfoliation of electric anode from the current collector, resulting in poor cycling performance and loss of capacity [18].

To minimize the effect of the volumetric change on electrochemical performance of Sb-based LIBs, various methods, including the use of nano- and/or microstructures, have been proposed. One of the methods is to incorporate inactive elements, such as Co [19], Fe [20], Cu [21], Mo [22] and Ni [23], in Sb-based nanomaterials, which can accommodate the volumetric change during lithiation/delitation. However, this method leads to the decrease of specific capacity due to the loss of active sites to the inactive components, and reduces the efficiency for energy storage. An effective method is to construct hollow or porous nanostructure, which can provide enough space to accommodate and suppress the volumetric change during lithiation/delitation [16, 24-26]. Hou et al synthesized hollow NiSb nanospheres by galvanic replacement, and obtained a charge capacity of 420 mA h g<sup>-1</sup> after 50 cycles for the Li-ion half cells with the hollow NiSb nanospheres as anode material at a current density of 100 mA g<sup>-1</sup> [16]. Using the same approach, Hou et al later prepared hollow Sb nanospheres, and achieved a charge capacity of 622.2 mA h g<sup>-1</sup> at a current density of 50 mA g<sup>-1</sup> for the Li-ion half cells with the hollow Sb nanospheres as anode material [26]. Such a large charge capacity can be attributed to the interior hollow structure of Sb nanospheres. Kim *et al* reported the synthesis of hollow Sb nanoparticles from SiO<sub>2</sub> template, and obtained a charge capacity of 587 mA h g<sup>-1</sup> at a current density of 120 mA g<sup>-1</sup> after 40 cycles for the Li-ion half cells with the hollow Sb nanospheres as anode material, which is higher than the 373 mA h g<sup>-1</sup> of Sb nanoparticles [24]. Using Sn–Sb–Cu hollow nanostructures as anode material in Li-ion half cells, Yang *et al* achieved a charge capacity of 390 mA h g<sup>-1</sup> at a current density of 100 mA g<sup>-1</sup> after 30 cycles, which is higher than the 180 mA h g<sup>-1</sup> of Sn–Sb–Cu nanoparticles [25]. All of these results reveal the important role of hollow structure in the storage of Li and the cycling stability of LIBs.

There are reports that materials consisting of Sb and carbon can efficiently restrain the volumetric change during lithiation/delithiation, and the Li-ion half cells with Sb/C as anode material have exhibited good cycling performance, because carbon can serve as conduction pathways and buffer to accommodate the volumetric change during lithiation/ delithiation [18, 27]. Currently, the anode materials made from Sb and carbon mainly include Sb/carbon fibers [28], Sb/carbon/graphite composite [29], Sb/graphite composite [30, 31], Sb/carbon nanocomposite [32] and Sb/carbon nanotube nanocomposite [33]. Park et al reported that the Liion half cells with anode made from Sb/carbon/graphite via the dispersion of Sb/carbon nanoparticles in carbon and graphite delivered a charge capacity of 460 mA h g<sup>-1</sup> at a current density of 100 mA g<sup>-1</sup> after 100 cycles [29]. Dailly *et al* synthesized Sb/graphite composites for LIBs, which possessed charge capacities of 420 mA h g<sup>-1</sup> after 35 cycles and 490 mA h g<sup>-1</sup> after 40 cycles at a current density of  $7\mu$ A mg<sup>-1</sup>, and noted that graphite can limit the pulverization of Sb and improve the cycling stability of Sb [30, 31]. Hassoun et al studied the effect of Sb morphology on the electrochemical performance of nanostructured Sb-C, and obtained a charge capacity of 450 mA h g<sup>-1</sup> at a current density of 100 mA cm<sup>-2</sup> after 100 cycles for the Li-ion half cells with the nanostructured Sb-C of 'optimized' morphology [32]. Using the Sb/carbon nanotubes synthesized by chemical reduction as the electric anode of LIBs, Chen et al demonstrated that the Li-ion half cells with the Sb/carbon nanotubes have larger charge capacities and better cycling stability than those with Sb only as the electric anode due to the buffer role of carbon nanotubes [33]. All of these studies have revealed that the composites of Sb and C can improve the cycling performance of the corresponding LIB systems, while none of the materials reported in the literature have utilized hollow carbon structure. Also, most studies have used carbon as the matrix with Sb dispersed in carbon, and there are a few studies focusing on the combination of Sb with carbon spheres structures. However, hollow carbon spheres, which function as conduction pathways and deformation buffer, can possess mechanical skeletons to support Sb-structures during discharge/charge cycles and limit the structural degradation/ damage of electric anode from the pulverization of Sb. Thus, it is of paramount importance to synthesize Sb(outer)-C (inner) structures, such as Sb-anchored hollow carbon



Figure 1. Illustration of the synthesis of Sb@HCMs.

microspheres, and investigate the electrochemical performance of the LIB system with the Sb(outer)–C(inner) structures as anode material.

In this work, we assemble Li-ion half cells and full cells with Sb nanocrystal-anchored hollow carbon microspheres (Sb@HCMs) as active-electrode material, and investigate the electrochemical performance of the Li-ion half cells and full cells. The Li-ion half cells exhibit a charge capacity of 605 mA h  $\,{\rm g}^{-1}$  after 100 cycles at a current density of 100 mA  $\,{\rm g}^{-1}$  and a charge capacity of 469.9 mA h  $\,{\rm g}^{-1}$  at a current density up to 1600 mA  $\,{\rm g}^{-1}$ , which is much higher than the theoretical capacity of 372 mA h  $\,{\rm g}^{-1}$  for commercial graphite electrode. The Li-ion full cells with Sb@HCMs//LiCoO2 deliver a charge capacity of 300 mA h  $\,{\rm g}^{-1}$  at a current density of 0.2 A  $\,{\rm g}^{-1}$  after 50 cycles.

# 2. Experimental details

### 2.1. Synthesis of hollow carbon microspheres (HCMs)

The materials used in this work were glucose, yeast extract, tryptone and glutaraldehyde. A light yellow solution consisting of 5 g of glucose, 2.5 g of yeast extract, 5 g of tryptone and 500 ml of deionized (DI) water, was prepared at 37 °C, and designated as the yeast culture medium. The yeast culture medium was sterilized in an autoclave (LS-50HG) at 115 °C for 103 min. A mixture of 0.1 g of dry yeast and 5 ml of the sterilized yeast culture medium was prepared and subjected to the irradiation of ultraviolet (UV) light for 30 min in a super clean bench. The UV-irradiated mixture was then poured into a clean sterilized tube, which was placed in a shaking-table concentrator at 37 °C for 24 h to form a suspension.

The suspension was centrifuged at 6000 rpm for 10 min, and the settled product in the tube was collected, and washed three times with NaCl solution (0.15 mM). The as-washed product was mixed with 10 ml of glutaraldehyde (2.5%) in a glass tube, which was placed in an oven overnight at 4 °C for the immobilization of the yeast cells. Ethanol with different volume fractions of 20%, 50%, 80%, 90% and 100% was used sequentially to dehydrate the immobilized yeast cells, and the dehydrated yeast cells were harvested by centrifugation and dried later in a vacuum oven. The obtained yeast cells were calcined at 300 °C for 2 h in air to form HCMs.

#### 2.2. Synthesis of Sb-anchored HCMs

A brown dark solution was prepared by magnetically stirring a mixture consisting of 0.1 g of the prepared HCMs, 0.8 g of SbCl<sub>3</sub> and 40 ml of ethylene glycol at 60 °C for 30 min, and a NaBH<sub>4</sub> solution with pH in a range of 12–14 was prepared by dissolving 0.4 g of NaBH<sub>4</sub> in 40 ml of DI water. Here, 5 M NaOH solution was used to control the pH of the NaBH<sub>4</sub> solution. Mixing the NaBH<sub>4</sub> solution with the brown dark solution and maintaining the mixture at 60 °C for 2 h yielded a suspension containing Sb@HCMs, from which they were collected by centrifugal separation at 8000 rpm for 10 min. The collected Sb@HCMs were washed five times with DI water and ethanol, respectively, and dried in a vacuum oven at 60 °C for 5 h. Figure 1 briefly summarizes the process for the synthesis of Sb@HCMs.

For comparison, Sb hollow microspheres (Sb HMs) were synthesized according to the method reported by Hou *et al* [34]. Briefly, a solution was prepared by adding 0.228 g of SbCl<sub>3</sub> to a well-dispersed suspension consisting of 0.104 g of Zn power and 60 ml of ethanol. The solution was exposed to ultrasound for 2 h to assist the chemical reaction for the formation of Sb HMs in the solution. HCl solution (1 mM) was then dripped into the solution to remove excessive Zn. The Sb HMs obtained from the solution by centrifugation were washed five times with ethanol, and dried in a vacuum oven at 60 °C for 5 h.

# 2.3. Characterization of microstructures

The morphology and chemical compositions of the specimens were analyzed on a field-emission scanning electron microscope (JEOL-JSM-7100F), and an energy-dispersive spectroscope (EDS, EDXA, XM20). X-ray diffraction (XRD) analysis of the specimens was performed from  $20^{\circ}-80^{\circ}$  at a scan rate of  $0.08^{\circ}$  per minute on a RigakuD/MAX-2500 (Rigaku, Japan) operating with Cu Ka ( $\lambda=1.54178$  Å). High-resolution transmission electron microscopy (HRTEM) imaging was conducted on a high-resolution transmission electron microscope (JEM-2010, JEOL, Japan). A thermogravimetric (TGA) test of the specimens was performed in air on a TG 151 thermal analyzer. The nitrogen adsorption–desorption isotherms were measured on a Quadrasorb SI surface area analyzer at 77 K.

#### 2.4. Electrochemical characterization

The Sb@HCMs were used as the active material of the working electrode in CR2032 coin-type half cells for electrochemical characterization. The materials in the working electrode consisted of 60 wt% active material (Sb@HCMs), 30 wt% of acetylene black carbon and 10 wt% of carboxymethyl cellulose (CMC); the current collector was a Cu plate of 0.15 mm in thickness. The working electrode was heattreated in a vacuum oven at 60 °C for 4 h, and the total mass of the active material of both Sb and carbon microspheres loaded in the working electrode was in a range of 1.0–1.1 mg. For comparison, both the HCMs and Sb HMs were also used as the active material of the working electrode, respectively, in CR2032 coin-type half cells for electrochemical analysis.

The counter electrode in the CR2032 coin-type half cells was Li-metal foil, and the separator was a Celgard 2400 (Celgard, LLC, Charlotte, NC). The electrolyte was 1 M LiPF<sub>6</sub> in carbonate(EC)/dimethyl carbonate(DMC)/diethyl-carbonate(DEC) with the volume ratio of 1:1:1. Cyclic voltammetric (CV) measurement of the half cells was conducted in a voltage range of 0.01–2.0 V versus Li<sup>+</sup>/Li at a scan rate of 0.1 mV s<sup>-1</sup> on a CHI-660 electrochemical workstation. Galvanostatic charge–discharge (GC) cycling and the rate stability of the half cells were studied on a battery test system (Land-CT2001A) in a voltage range of 0.01–2.0 V, and the electrochemical impedance spectroscopy (EIS) analysis of the half cells was performed on a CHI-660 electrochemical workstation in a frequency range of 10 mHz–100 kHz at an AC of 5 mV amplitude.

Li-ion full cells with the anode made from the Sb@HCMs were constructed. The cathode consisted of LiCoO<sub>2</sub>, acetylene black and polyvinylidene fluoride (PVDF) with the weight ratio of 80:10:10. Al foil was used as the current collector of the cathode. The weight ratio of the active materials (Sb@HCMs:LiCoO<sub>2</sub>) in the Li-ion full cells was 1:1.2. The GC cycling of the full cells was performed in a voltage range of 1.8–3.7 V on a battery test system (Land-CT2001A). The energy density was calculated on the total mass of all the active materials.

#### 3. Results and discussion

Figure 2 shows the SEM images of cultivated yeast cells, HCMs (300 °C), Sb@HCMs (300 °C) and elemental mapping of the Sb@HCMs. It is evident that the cultivated yeast cells (figure 2(a)) are relatively uniform and present in a nearly spherical shape with size in a range of 4.3–4.7  $\mu$ m. After the calcination at 300 °C, the cultivated yeast cells were converted to carbon microspheres also with a nearly spherical shape (figure 2(b)). The surface of the carbon microspheres is much smoother than the cultivated yeast cells, and the average size of the carbon microspheres is  $\sim$ 2.5  $\mu$ m, smaller than that of the yeast cells. The hollow structure of HCMs is observed from the TEM image in figure S1, which is available online at stacks.iop.org/NANO/31/135404/mmedia in the supporting information. Such a result is due to the combustion

of bio-macromolecules in the yeast cells during the calcination, leading to the removal of bio-macromolecules and the formation of hollow structure [35]. The calcination of yeast cells at temperatures of 400 °C and 500 °C caused the formed carbon microspheres to stick together, and the calcination at temperature of 600 °C destroyed the sphere-like framework of the yeast cells due to excessive carbonization (figure S2 in the supporting information). Figure S3 in the supporting information shows the SEM image of the HCMs prepared from dry yeast cells at 300 °C. The carbonized yeast cells sintered together without the presence of individual carbon microspheres.

Figures 2(c) and (d) depicts the SEM images of the Sb@HCMs derived from the yeast cells calcined at 300 °C. It is evident that numerous Sb nanoparticles (inset of figure 2(d)) stacked over the surfaces of the HCMs. Depending on the amount of SbCl<sub>3</sub> in the solution, the surfaces of the HCMs were covered either partially or completely by Sb nanoparticles. For the Sb@HCMs with full cover of Sb nanoparticles, the Sb nanoparticles formed a porous layer of  $\sim 1.5 \ \mu m$  on the surfaces of the HCMs, as estimated from the enlarged SEM image (figure 2(d)). The porous structure can reduce the migration distance of Li-ions and likely improve the structural stability of the Sb nanoparticles during lithiation/delithiation [36]. Also, the surface stresses on the Sb nanoparticles can confine the deformation and limit the magnitude of the stresses produced in the Sb nanoparticles due to lithiation/delithiation, which can improve the structural integrity and cycle stability of the Sb nanoparticles upon electrochemical cycling [37, 38]. Figure 2(e) shows the elemental mapping of Sb, C and N over the Sb@HCMs. Sb, C and N were statistically uniformly distributed. Note that high N-content can improve the reactivity and capacity of carbon [39]. For comparison, figure S4 in the supporting information shows the SEM images and EDS mapping of the Sb@HCMs and the mixture of Sb nanoparticles and carbon microspheres. There exist regions with depletion of Sb in the mixture of Sb nanoparticles and carbon microspheres. Figure S5 in the supporting information shows the SEM and TEM images of the Sb HMs. The Sb HMs are porous, and are present in a sphere-like shape.

The surface characteristics of the porous structure of the Sb@HCMs were analyzed by N2 adsorption-desorption isotherms. Figure 3 shows the N2 adsorption and desorption isotherms of the Sb@HCMs and the distribution of the corresponding pore sizes calculated from the adsorption isotherms. The adsorption and desorption isotherms exhibit Type II feature. There exists a large increase of adsorption at large relative pressure, suggesting the presence of large pores (interior and hollow voids) in the Sb@HCMs [8, 40]. Using the Brunauer-Emmett-Teller method, the specific surface area of the Sb@HCMs is calculated to be 24.04  $\text{m}^2\cdot\text{g}^{-1}$  with a pore volume of  $0.16\,\text{cm}^3\cdot\text{g}^{-1}$ . The distribution of the pore sizes, as shown in figure 3(b), reveals that the sizes of most pores are in the range of 45-120 nm. Such a size distribution suggests that there likely exist hierarchical pore structures in the Sb@HCMs, which can facilitate the motion of Li<sup>+</sup> and e<sup>-</sup> and provide enough space for the storage of Li [41]. Also, the

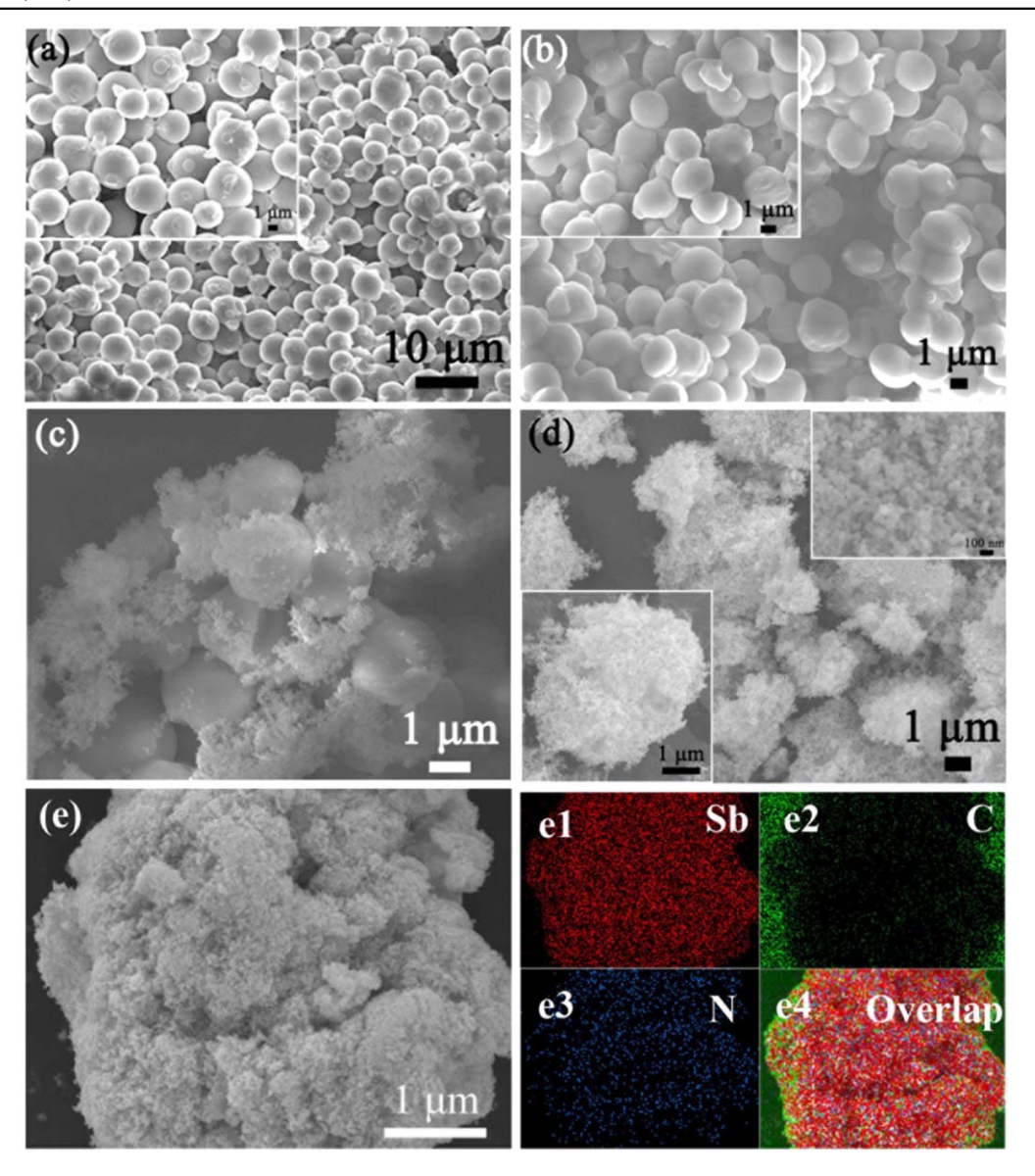


Figure 2. SEM images of (a) cultivated yeast cells, (b) HCMs (calcination temperature:  $300\,^{\circ}$ C) and (c)–(d) Sb@HCMs (calcination temperature:  $300\,^{\circ}$ C); (e) elemental mapping of Sb@HCMs: (e1) Sb, (e2) C, (e3) N and (e4) superposition of all elements.

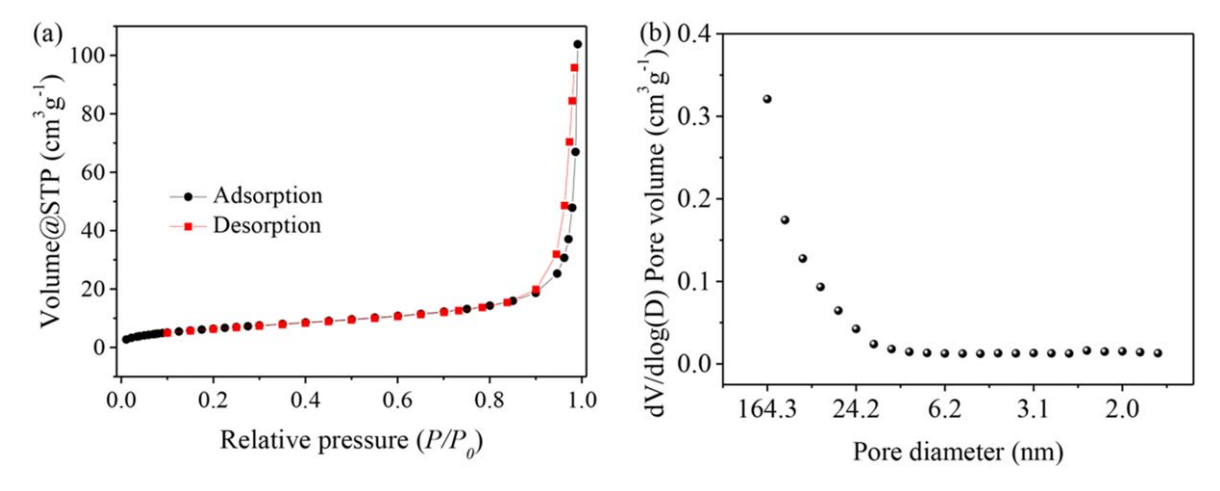


Figure 3. (a)  $N_2$  adsorption and desorption isotherms of the Sb@HCMs and (b) distribution of the corresponding pore sizes calculated from the adsorption isotherms.

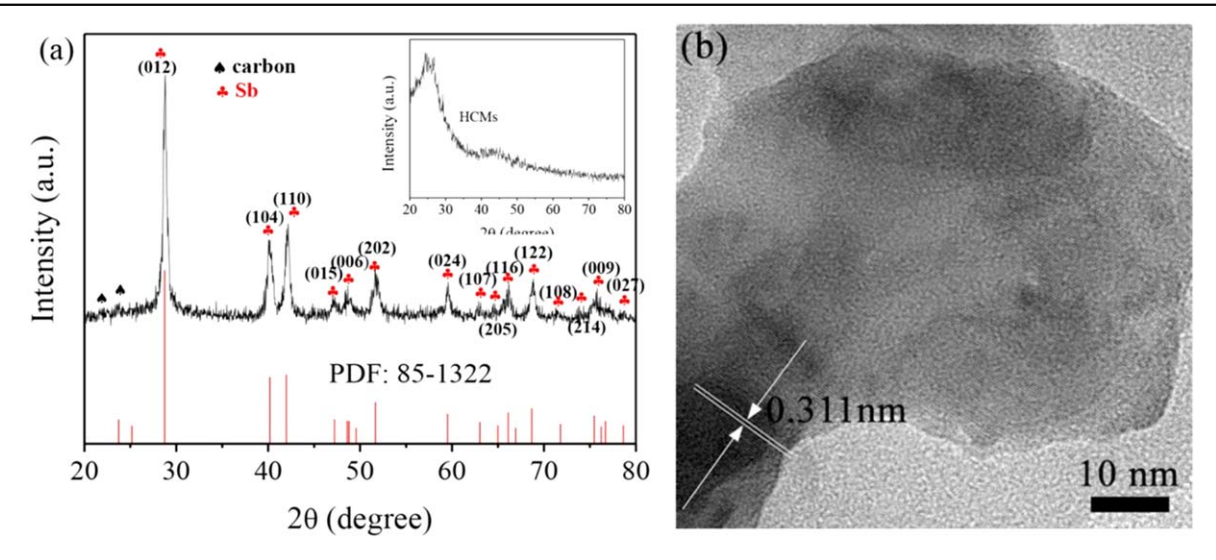


Figure 4. (a) XRD patterns of the Sb@HCMs and HCMs (calcination temperature: 300 °C) and (b) HRTEM image of a Sb nanoparticle in the Sb@HCMs.

hierarchical pore structures can accommodate the volumetric change induced by lithiation/delithiation during electrochemical cycling [42].

Figure 4(a) shows the XRD pattern of the Sb@HCMs. There exist strong diffraction peaks corresponding to the rhombohedral structure of Sb (R-3m, JCPDS card no. 85-1322), and there are no diffraction peaks representing the structure of Sb oxide. The strong and relatively broad diffraction peaks suggest that the Sb in the Sb@HCMs is nanocrystal. The lattice constants are estimated to be a = b = 0.431 nm and c = 1.130 nm, which match the values in the standard PDF card (No. 85-1322). Using the full pattern Rietveld refinement method (Jade 6, Materials Data, Inc.), the average size of the Sb crystals in the Sb@HCMs is estimated to be  $\sim$ 19 nm, implying that the Sb nanoparticles were nanocrystals in the Sb@HCMs. The XRD pattern of the HCMs (calcination temperature: 300 °C), as shown by the inset in figure 4(a), reveals weak and broad diffraction peaks at 25.19° and 43.12° of the (002) and (100) lattice planes of carbon, respectively, suggesting that the HCMs were at a state of low graphitization [43]. The asymmetry of the diffraction peak of the (002) plane indicates the coexistence of both disordered and crystalline structures in the HCMs. Figure S6 and table S1 in the supporting information summarize the structural information of the HCMs, which confirms the presence of both disordered and crystalline structures in all the HCMs synthesized in this work. Figure 4(b) depicts an HRTEM image of the Sb in the Sb@HCMs. There are wellresolved (012) lattice fringes (d = 0.311 nm) of rhombohedral Sb in accord with the XRD pattern shown in figure 4(a).

TGA analysis of the Sb@HCMs was performed to determine the weight fraction of Sb in the Sb@HCMs. Figure 5(a) shows the TGA curve of the Sb@HCMs. There is an abrupt drop in the normalized weight around  $600\,^{\circ}$ C, at which the HCMs were burned off and Sb was oxidized to form Sb<sub>2</sub>O<sub>4</sub>, as confirmed by the XRD pattern of the combustion product shown in figure 5(b). According to figure 5(b), all the diffraction peaks represent the structure of

 $Sb_2O_4$  (JCPDS card no. 17-0620). The weight fraction of Sb in the Sb@HCMs can be calculated from the final weight of  $Sb_2O_4$  as,

$$\begin{split} Sb(\%) &= \frac{2 \times \text{molecular weight of Sb}}{\text{molecular weight of Sb}_2O_4} \\ &\times \frac{\text{final weight of Sb}_2O_4}{\text{initial weight of Sb@HCMs}} \times 100. \end{split}$$

Using the mass change of the Sb@HCMs during the TGA measurement and the above equation, the weight fraction of Sb in the Sb@HCMs is found to be  $\sim$ 63.35%. Using the weight fraction of  $\sim$ 63.35% for Sb in the Sb@HCMs, the mass loading of Sb in the working electrode is calculated to be in the range of 42.20–50.64 mg  $\cdot$  cm<sup>-2</sup>, which is suitable for practical applications [44].

Figure 6(a) shows the CV curves of the first three cycles for the half cells with the Sb@HCMs as the working electrode. There is a broad peak (reduction peak) around 0.69 V (0.5-0.9 V) during the first cathodic sweeping, which is attributed to the formation of a layer of solid electrolyte interphase (SEI) on the surfaces of the Sb@HCMs due to the decomposition of electrolyte, the first lithiation of Sb to form  $\text{Li}_{x}\text{Sb}$  (Sb + xLi<sup>+</sup> + xe<sup>-</sup>  $\leftrightarrow$  Li<sub>x</sub>Sb, 0  $\leqslant$  x  $\leqslant$  3) [26, 45] and the lithiation of the HCMs. The SEI layer caused the loss of capacity during the first cycle. The reduction peak shifts to 0.71 V for the second cathodic sweeping. Note that a similar shift has been observed for a Na-ion battery with Sb/carbon composite as the working electrode [46, 47]. There is a weak peak presented at 1.2 V during the sweeping, which disappeared in the subsequent sweeps. Such behavior is likely associated with the irreversible delithiation of residual impurities in the HCMs [32, 48]. After the first sweep, a new peak at 0.81 V is present for the subsequent lithiation, and is attributed to the formation of Li<sub>3</sub>Sb [11]. For the delithiation, there is one peak at 1.1 V (0.9–1.2 V), corresponding to the delithiation conversion of Li<sub>3</sub>Sb to Sb [45]. After the first cycle, the CV curves for the subsequent cycles remain

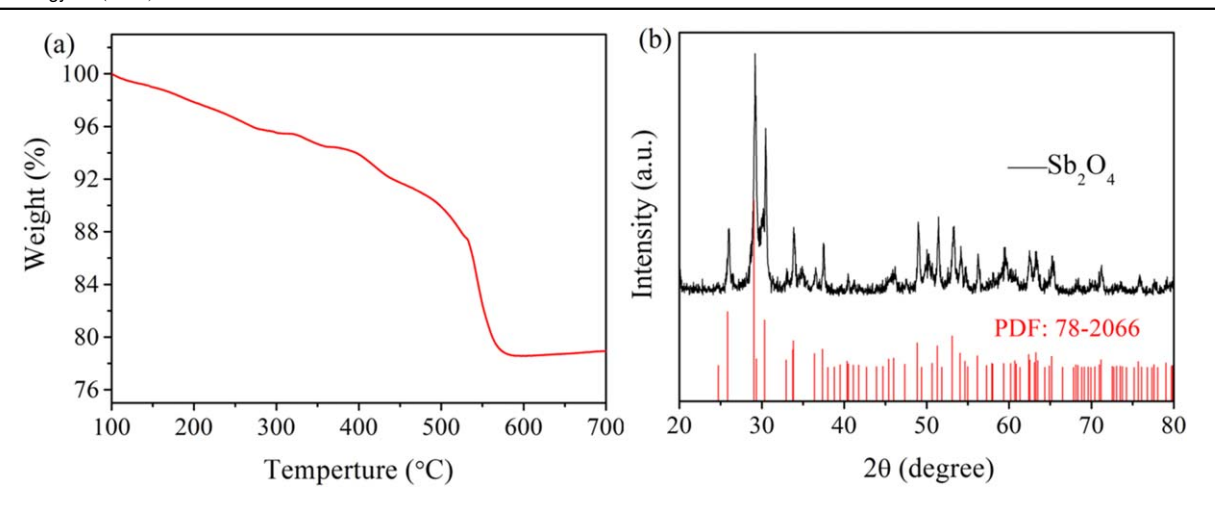
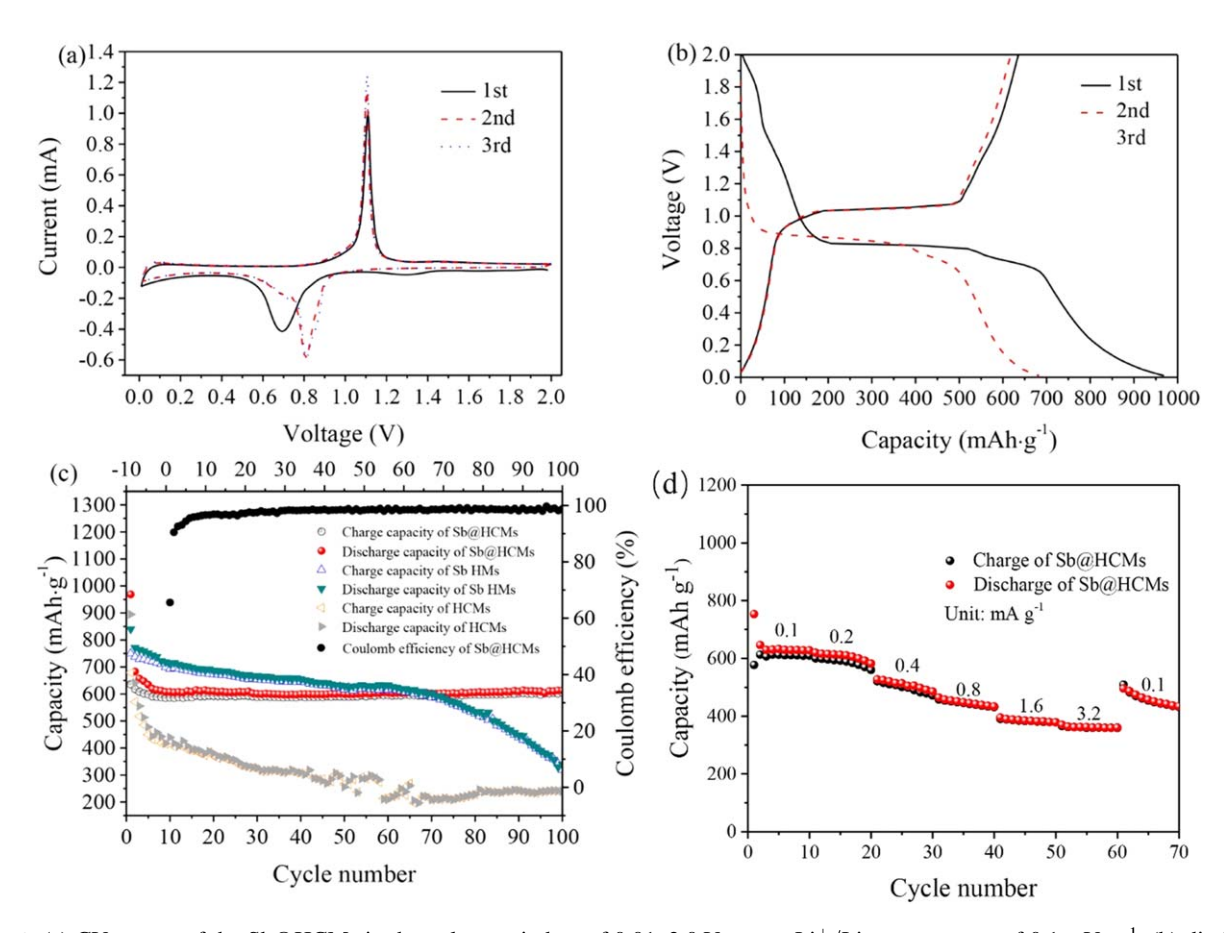


Figure 5. (a) TGA curve of the Sb@HCMs and (b) XRD spectrum of the combustion product of the Sb@HCMs.



**Figure 6.** (a) CV curves of the Sb@HCMs in the voltage window of 0.01-2.0 V versus  $\text{Li}^+/\text{Li}$  at a scan rate of  $0.1 \text{ mV s}^{-1}$ , (b) discharge-charge curves of the Sb@HCMs in the voltage window of 0.01-2.0 V versus  $\text{Li}^+/\text{Li}$  at a current density of  $100 \text{ mA g}^{-1}$ , (c) cycling performance of the Sb@HCMs, HCMs and Sb HMs at a current density of  $100 \text{ mA g}^{-1}$  and Coulombic efficiency of the Sb@HCMs, and (d) rate performance of the Sb@HCMs.

relatively the same, suggesting excellent reversibility of the electrochemical charging and discharging for the half cells with the Sb@HCMs as the working electrode.

Figure 6(b) shows the discharge-charge curves for the first three cycles of the half cells with the Sb@HCMs as the working electrode at a current density of 100 mA g<sup>-1</sup>. There is a long and oblique plateau, over which the voltage decreases gradually in the range of 0.6–0.85 V for the

lithiation in the first cycle, representing the formation of an SEI layer and the lithiation of Sb to form Li<sub>x</sub>Sb ( $0 \le x \le 3$ ). For the subsequent discharge cycles, the voltage for the plateau is in the range of 0.69–0.90 V, corresponding to the formation of Li<sub>3</sub>Sb during the lithiation. For the charging process of all the electrochemical cycles, there is a plateau at 1.05 V, corresponding to the delithiation of Li<sub>3</sub>Sb to form Sb. The plateaus presented in

the discharge-charge curves are in accordance with the peaks presented in the CV curves.

According to figure 6(b), the discharge capacity of the Sb@HCMs is 968.6 mA h  $g^{-1}$  for the first cycle  $(>660 \text{ mA h g}^{-1})$ , about 1.5 times the theoretical capacity of Sb. There likely existed some side reactions, including the formation of SEI, involved in the first discharge. The initial charge capacity of the Sb@HCMs is  $\sim$ 635.6 mA h g<sup>-1</sup> with a low Coulombic efficiency of 65.6%, indicating large loss of capacity during the first cycle likely due to the formation of the SEI layer on the surfaces of the Sb and HCMs. The decrease of the charge capacity in the subsequent cycles reveals the irreversible decomposition of Li<sub>x</sub>Sb [32], while the Coulombic efficiency becomes more than 97% after the 30th cycle. It needs to be pointed out that the electrochemical performance of the half cells with the Sb@HCMs as the working electrode was also investigated at a current density of 500 mA g<sup>-1</sup>, as shown in figure S7 in the supporting information. The voltage plateaus similar to those at a current density of 100 mA g<sup>-1</sup> are also observed.

The cycling behavior of the half cells made, respectively, from the Sb@HCMs, HCMs and Sb HMs was examined at a current density of 100 mA g<sup>-1</sup>. The variations of the charge and discharge capacities with the cycle number of electrochemical cycling at a current density of 100 mA g<sup>-1</sup> are shown in figure 6(c). According to figure 6(c), the half cells with the Sb HMs as the working electrode have the highest reversible capacity between the second cycle and fiftieth cycle, and fast fade of the capacity to 330 mA h g<sup>-1</sup> over 100 cycles. This poor cycling performance is due to the irreversible lithiation and delithiation between Sb and LixSb [33]. The capacity of the half cells with the HCMs calcined at 300 °C (figure S8 in the supporting information) gradually and slowly decreases with the increase of the cycle number for the first 50 cycles, attributed to the stabilization of the SEI layer and irreversible lithiation of the HCMs in low graphitic regions [48] (see figure S6 and table S1 in the supporting information). For the electrochemical cycling with the cycle number larger than 100, the charge capacity of the half cells with the HCMs is only 238 mA h  $g^{-1}$ . As shown in figure S8 in the supporting information, similar behavior for the half cells with the HCMs calcined at 400 °C, 500 °C and 600 °C has been observed. There is no significant difference in the cycling performance between the half cells with the HCMs calcined at different temperatures. Comparing the capacities of the half cells with the HCM or Sb HM working electrode with those with the Sb@HCM as the working electrode, we conclude that the half cells with the Sb@HCMs have excellent cycling performance under the same cycling conditions. There is always loss of capacity for the first five cycles for all the half cells, which is common behavior for LIBs due to the formation of a stable SEI layer [16]. For the half cells with the Sb@HCMs, there is only an  $\sim$ 8% drop of the charge capacity in comparison with the initial charge capacity for the tenth and subsequent cycling. The half cells with the Sb@HCMs exhibit excellent cycling performance.

It is interesting to note that the capacity of the half cells with the Sb@HCMs increases slightly and stably after the

40th cycle, and reaches a plateau of 605.5 mA h g<sup>-1</sup> after 100 cycles, which is 95.2% of the initial charge capacity. There is a 3.2% increase in the charge capacity. Such behavior can be attributed to the increase in the interlayer distance between carbon layers during cyclic lithiation and delithiation, resulting in fast charge transfer and the increase of the electrode capacity with increasing numbers of cycles [39]. From figures 6(c) and S9, we note that the charge capacities of the half cells with the acetylene black and HCMs are 140 and 238 mA h g<sup>-1</sup>, respectively, under the same cycling condition. Using the law of mixture, the reversible capacity of the Sb@HCMs is estimated to be  $\sim$ 535.5 mA h g<sup>-1</sup>. Figure S10 shows the electrochemical performance of the two groups of materials consisting of Sb nanoparticles and HCMs. One is the physically mixed Sb nanocrystals and HCMs, which was used in Li-ion half cells; the other one is the Sb@HCMs, which reduces the fraction of acetylene black. It is evident that the Li-ion half cells with the Sb@HCMs exhibited better stability and electrochemical performance than those with the physical mixture of Sb nanocrystals and HCMs. That is to say, the Sb@HCMs is not a simple mixture of Sb nanocrystals and HCMs.

The rate performance of the half cells with the Sb@HCMs as the working electrode was investigated. Figure 6(d) and table 1 summarize the rate performance of the half cells with the Sb@HCMs as the working electrode at current densities of 100, 200, 400, 800, 1600 and  $3200 \, \text{mA g}^{-1}$ . The half cells possess reversible capacities of 610, 582.1, 485.6, 433.9, 379 and 360.7 mA h g $^{-1}$ , respectively, for the corresponding current densities, which are much larger than the theoretical capacity of  $372 \text{ mA h g}^{-1}$  for commercial graphite electrode for the current densities less than or equal to  $800 \,\mathrm{mA \, g^{-1}}$ , as expected, due to the contribution of the Sb nanocrystals. For the current density decreasing to 100 mA g<sup>-1</sup>, the reversible capacity recovered to 71.1% of the initial charge capacity. Such results demonstrate that the Li-ion batteries with the Sb@HCMs as active material can maintain reasonable energy storage when there are large variations in the charge-discharge current density.

For comparison, table 1 also lists the rate performance reported in the literature for the half cells with Sb/carbon composite as the working electrode. It is evident that the half cells with the Sb@HCMs as electrode material have better cycling performance than most of the half cells reported in the literature and comparable rate performance.

The EIS analyses of the half cells with the Sb@HCMs and Sb HMs as the working electrode were conducted, and the equivalent circuits in figure 7(a) were used to fit the Nyquist plots of the Sb@HCMs and Sb HMs, respectively. It is evident that both the Nyquist plots consist of an oblique semicircle in the region of high frequency, which can be described by the electron transfer resistance ( $R_{\rm ct}$ ) and the resultant resistance ( $R_{\rm s}$ ) of the SEI layer and contact resistance in the equivalent circuit, respectively. The linear portion in the region of middle frequency with a slope of  $\sim$ 1 represents the Warburg impedance ( $Z_{\rm w}$ ) in the equivalent circuit, which is associated with the migration of Li-ions in

Table 1. Comparison of electrochemical performance of electrodes made from Sb/carbon composites.

Anode materials	Cycling performance (mA h g <sup>-1</sup> )	Rate capacity (mA h g <sup>-1</sup> )	Reference
Sb@HCMs	605 at 100 mA g <sup>-1</sup> after 100 cycles;	610 at 100 mA g <sup>-1</sup> ;	This work
	$405 \text{ at } 500 \text{ mA g}^{-1} \text{ after } 100 \text{ cycles}$	$582.1 \text{ at } 200 \text{ mA g}^{-1};$	
		$485.6 \text{ at } 400 \text{ mA g}^{-1};$	
		433.9 at 800 mA $g^{-1}$ ;	
		379 at 1600 mA $g^{-1}$ ;	
		$360.7 \text{ at } 3200 \text{ mA g}^{-1}$	
Sb/carbon	550 at 230 mA $g^{-1}$ after 500 cycles	595 at 115 mA $g^{-1}$ ;	[18]
		547 at 230 mA $g^{-1}$ ;	
		498 at 575 mA $g^{-1}$ ;	
		424 at $1150 \text{ mA g}^{-1}$ ;	
	,	$317 \text{ at } 2300 \text{ mA g}^{-1}$	
Sb/carbon nanotube	287 at $50 \mathrm{mA g}^{-1}$ after 30 cycles	N/A	[33]
SnSb <sub>0.5</sub> /carbon nanotube	369 at $50 \text{ mA g}^{-1}$ after 30 cycles	N/A	[33]
Sb/graphite	420 at 7 mA $g^{-1}$ after 35 cycles	N/A	[30]
Sb/mesophase carbon microbeads	420 at $0.2 \text{ mA cm}^{-2}$ after 25 cycles	N/A	[49]
Sb/graphene nanosheet	714 and 896 at 80 mA $g^{-1}$ after 30 cycles	660–700 at 1600 mA $g^{-1}$ ;	[50]
		$400-450$ at $4000 \mathrm{mA g}^{-1}$	
Sb/graphite	490 at 0.007 mA $g^{-1}$ after 40 cycles	N/A	[31]
Sb-C nanocomposite	200 at $100 \text{ mA cm}^{-2} \text{ g}^{-1}$ after $100 \text{ cycles}$	N/A	[32]
Sb/carbon composite fibers	315.9 at $100 \text{ mA g}^{-1}$ after $100 \text{ cycles}$	$464.4 \text{ at } 100 \text{ mA g}^{-1};$	[51]
		395.4 at 200 mA $g^{-1}$ ;	
		328 at $400 \text{ mA g}^{-1}$ ;	
		246.2 at 800 mA $g^{-1}$ ;	
	-1 -1 -1 -1	149.8 at 1600 mA g <sup>-1</sup>	5007
Sb/carbon	330 at 100 mA $g^{-1}$ after 100 cycles;	N/A	[29]
	350 at 105 mA $g^{-1}$ after 150 cycles;		
	350 at 350 mA g <sup>-1</sup> after 100 cycles;		
Ch /h/h:t-	350 at 700 mA $g^{-1}$ after 60 cycles.	NI / A	[20]
Sb/carbon/graphite	460 at $100 \text{ mA g}^{-1}$ after $100 \text{ cycles}$	N/A	[29]

the electrode [50]. The constant phase element (CPE) element, with an index of n (0< n < 1) in the circuit, is used to describe the dispersion effect in the electrode.

Using the equivalent circuit to curve-fit the Nyquist plots in figure 7(a), we obtain electron transfer resistances of 70 and  $120~\Omega$  for the Sb@HCMs and Sb HMs, respectively. The small electron transfer resistance of the Sb@HCMs suggests rapid migration of Li in the Sb@HCMs, which is beneficial for the capacity recovery of the Sb@HCM-based electrode and the improvement of the rate performance of LIBs. The n values of the CPE elements are (0.76, 0.66) and 0.73 for the Sb@HCMs and Sb HMs, respectively, suggesting that the Sb@HCMs possess better capacitive characteristic than the Sb HMs. Note that 0 and 1 of the n value correspond to resistive element and capacitive element, respectively.

Figure 7(b) shows the variation of resistive impedance with the square root of frequency. The resistive impedance is a linearly increasing function of the reciprocal of the square root of frequency. Using the relationship given by Guo *et al* [52], the diffusion coefficients for Li migration in the Sb@HCMs and Sb HMs are estimated to be  $3.26 \times 10^{-24} \, \mathrm{cm}^2 \, \mathrm{s}^{-1}$  and  $1.39 \times 10^{-24} \, \mathrm{cm}^2 \, \mathrm{s}^{-1}$ , respectively, suggesting the faster migration of Li-ion in the Sb@HCMs than in Sb HMs.

Figure 7(c) shows the CV curves at various scan rates ranging from  $0.2-1.0 \,\mathrm{mV \, s^{-1}}$ . There is one anode peak

(Peak 1) and one cathodic peak (Peak 2). The peak current (i) as a function of the scan rate (v) can be expressed as [39],

$$i = av^b$$
,

where a and b are parameters. The  $\mathrm{Li}^+$  storage mechanism can be illustrated by the value of b. For b=0.5, the diffusion mechanism is dominant; for b=1.0, it means the capacitive behavior is dominant. Figure 7(d) shows the variation of the peak current with the scan rate, from which we obtain the b values as 0.518 and 0.653 for Peak 1 and Peak 2, respectively, suggesting that the diffusion process contributes to the storage of Li in the Li-ion half cells.

Considering the practical applications of Sb@HCMs in the energy storage, we assembled Li-ion full cells with the Sb@HCMs as the anode and commercial LiCoO<sub>2</sub> as the cathode, and examined the electrochemical performance of the Li-ion full cells. The charge capacity of the LiCoO<sub>2</sub> is  $104 \, \text{mA} \, \text{h} \, \text{g}^{-1}$  after  $100 \, \text{cycles}$  at a current density of  $100 \, \text{mA} \, \text{g}^{-1}$ , and there is a voltage plateau of  $3.85 \, \text{V}$  (see figure S11 in the supporting information).

The Li-ion full cells were used to power several electronic devices, as schematically shown in figure 8(a). Figure 8(b) shows the discharge–charge curves at a current density of 200 mA g<sup>-1</sup> for the first three cycles. The large difference between the first curve and second or third curve is due to the formation of the SEI layer in the first cycle. There

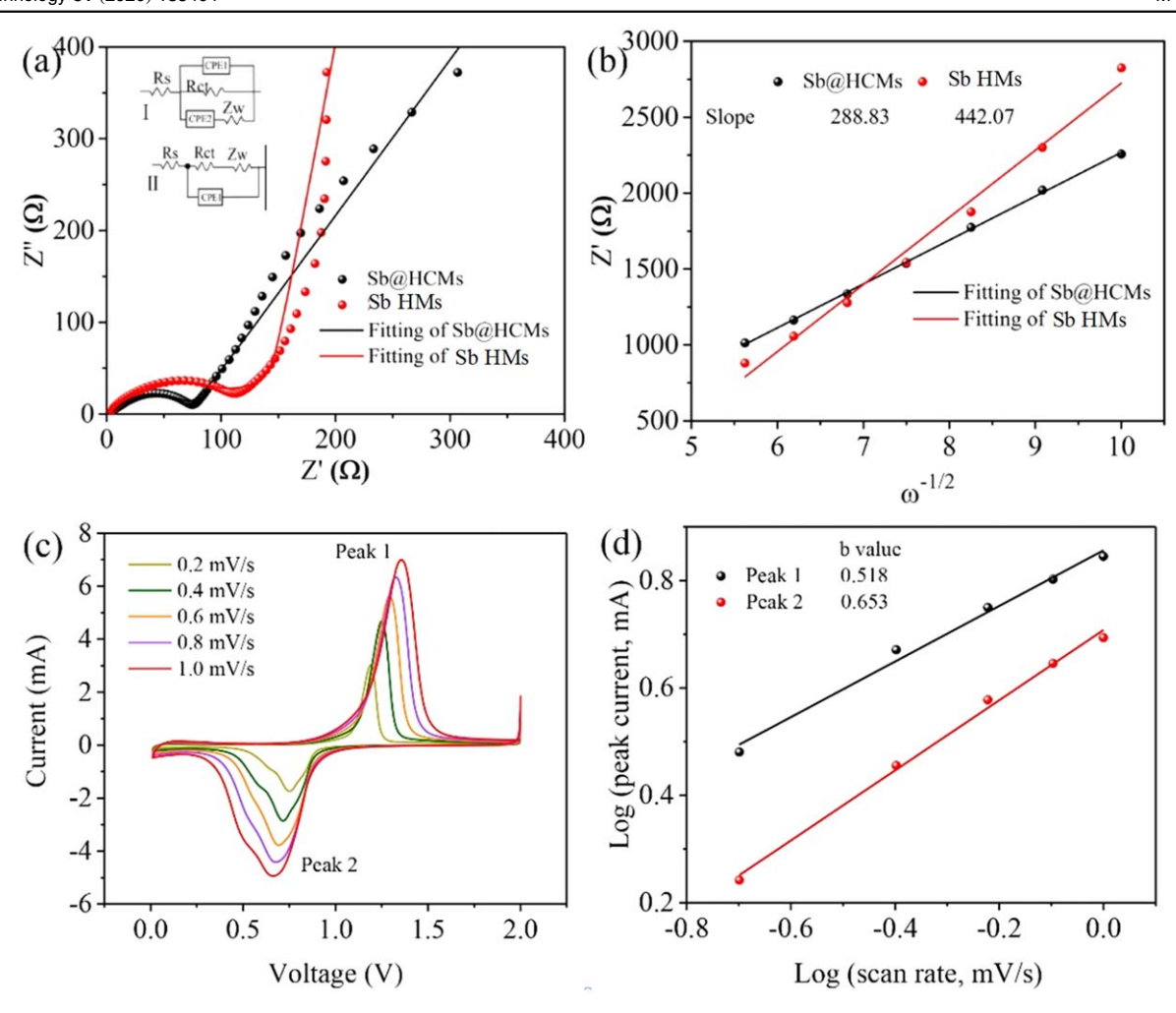


**Figure 7.** (a) Nyquist plots of Sb@HCMs and Sb HMs with equivalent circuits, (b) variation of resistive impedance with square root of frequency, (c) CV curves at various scan rates in the range of  $0.2-1.0 \text{ mV s}^{-1}$  and (d) b values.

is no significant difference between the second curve and third curve, suggesting excellent cycle stability of the full cells. The Li-ion full cells with Sb@HCMs//LiCoO<sub>2</sub> successfully powered light-emitting diodes (inset of figure 8(c)) with electric voltage of 2 V and power of 20 mW. Figures 8(c) and (d) show the cycling and rate performance of the Li-ion full cells with Sb@HCMs//LiCoO<sub>2</sub>, respectively. It is evident that the Li-ion full cells possessed a charge capacity of  $\sim\!300$  mA h g $^{-1}$  after 50 cycles at a relatively high current density of 0.2 A g $^{-1}$ , and the retentions of the charge capacity are 510, 394.7, 302, 179.8 and 270.2 mA h g $^{-1}$  at the current densities of 0.1, 0.2, 0.4, 0.8 and 0.1 A g $^{-1}$ , respectively.

### 4. Summary

In summary, we have successfully synthesized Sb-anchored hollow carbon microspheres using the calcination of cultivated yeast cells and the reduction of SbCl<sub>3</sub> in ethylene glycol solution on the surface of hollow carbon microspheres. The surface properties and microstructures of the Sb-anchored hollow carbon microspheres have been

systematically characterized. Using the Sb-anchored hollow carbon microspheres as the active-electrode material, we have assembled Li-ion half cells and Li-ion full cells, and investigated the electrochemical performance of the Li-ion half cells and Li-ion full cells. The results are summarized as follows.

- 1. The Sb-anchored hollow carbon microspheres possess hollow and porous structure, and the Sb nanoparticles in the Sb-anchored hollow carbon microspheres are nanocrystals.
- 2. The Li-ion half cells with the Sb-anchored hollow carbon microspheres as the working electrode exhibit excellent cycle stability and great rate performance, and have charge capacities of 605 mA h g<sup>-1</sup> for electrochemical cycling over 100 cycles at a current density of 100 mA g<sup>-1</sup>, 405 mA h g<sup>-1</sup> at a current density of 500 mA g<sup>-1</sup> and 360.7 mA h g<sup>-1</sup> at a current density of 3200 mA g<sup>-1</sup>, respectively.
- 3. The Li-ion full cells with Sb@HCMs//LiCoO<sub>2</sub> possess a charge capacity of  $\sim$ 300 mA h g<sup>-1</sup> after 50 cycles at a relatively high current density of 200 mA g<sup>-1</sup>, and the

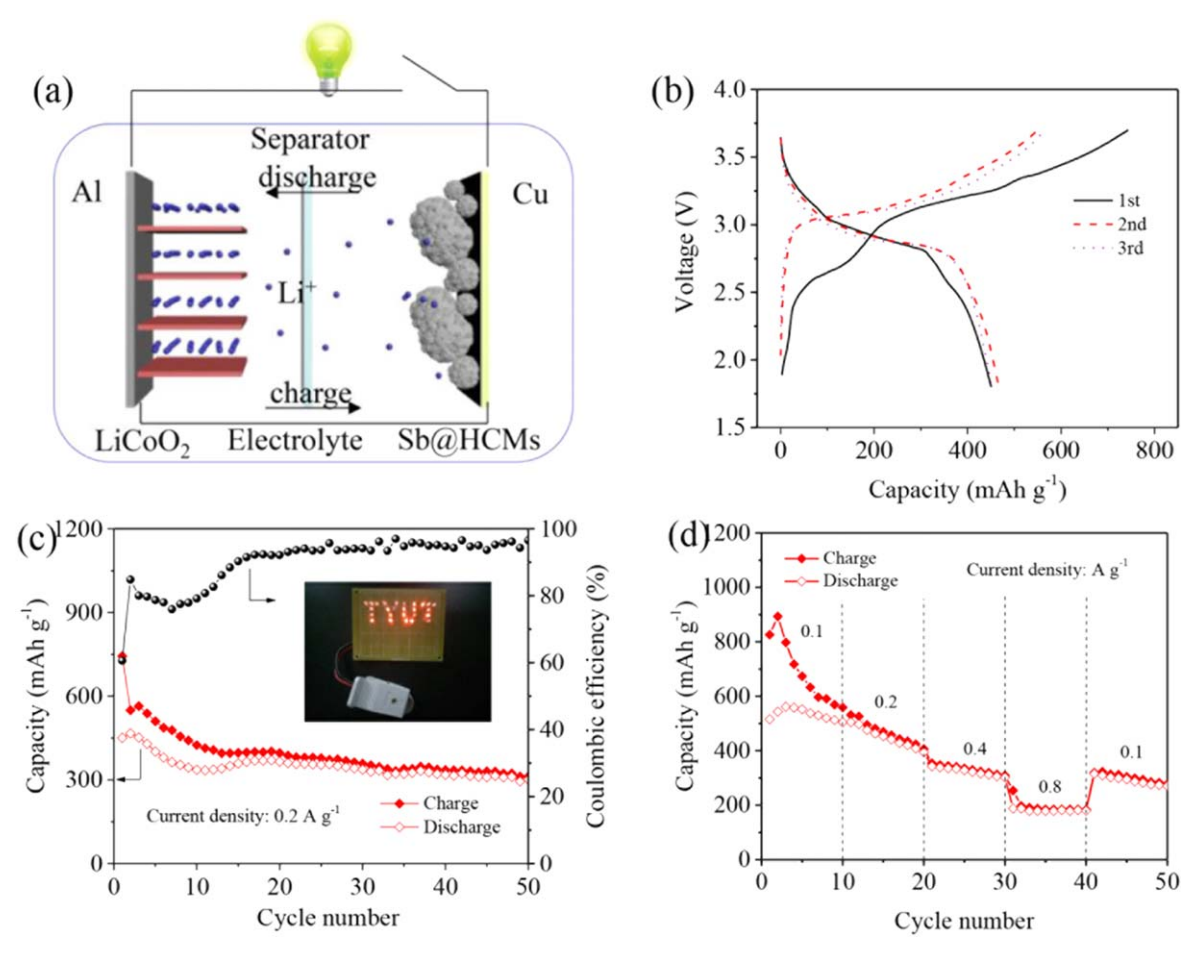


**Figure 8.** Electrochemical performance and applications of Li-ion full cells with  $Sb@HCMs//LiCoO_2$ : (a) schematic of Li-ion full cells, (b) discharge–charge curves at a current density of  $200 \text{ mA g}^{-1}$ , (c) electrochemical cycling (the inset is the diodes powered by a Li-ion full cell) and (d) rate performance.

retentions of the charge capacity are 510, 394.7, 302, 179.8 and 270.2 mA h  $\rm g^{-1}$  at current densities of 100, 200, 400, 800 and 100 mA  $\rm g^{-1}$ , respectively.

## **ORCID** iDs

Meiqing Guo https://orcid.org/0000-0003-1456-4889 Fuqian Yang https://orcid.org/0000-0001-6277-3082

# **Acknowledgments**

This work was supported by the National Natural Science Foundation of China (Grant nos. 51301117, 11502158 and 51671140), the International Cooperation Project Foundation of Shanxi Province, China (Grant nos. 201603D421037 and 2015081053), the Shanxi Provincial Foundation for Leaders of Disciplines in Science, China, the Top Young Academic Leaders of Shanxi and the '1331 project' Key Innovation Teams of Shanxi Province, the Higher School Science and Technology Innovation Project Foundation of Shanxi Province, China (Grant no. 2016128), the Shanxi Province Science Foundation (Grant no. 201801D121281) and the Research Project Supported by the Shanxi Scholarship Council of China (Grant no. 2015-034). FY is grateful for the support of the NSF through the grant CMMI-1634540, monitored by Dr Khershed Cooper.

# References

- [1] Liu H, Wei Z, He W and Zhao J 2017 Thermal issues about Liion batteries and recent progress in battery thermal management systems: a review *Energy Convers. Manage*. **150** 304–30
- [2] Bai Z, Fan N, Sun C, Ju Z, Guo C, Yang J and Qian Y 2013 Facile synthesis of loaf-like ZnMn<sub>2</sub>O<sub>4</sub> nanorods and their excellent performance in Li-ion batteries *Nanoscale* 5 2442–7
- [3] Goriparti S, Miele E, De Angelis F, Di Fabrizio E, Zaccaria R P and Capiglia C 2014 Review on recent progress of nanostructured anode materials for Li-ion batteries J. Power Sources 257 421–43
- [4] Scrosati B and Garche J 2010 Lithium batteries: status, prospects and future J. Power Sources 195 2419–30
- [5] Zhang Y, Lundblad A, Campana P E and Yan J Y 2016 Employing battery storage to increase photovoltaic selfsufficiency in a residential building of Sweden *Energy Procedia* 88 455–61

- [6] Guo M, Zhang X, Bai Z, Ye J, Meng W, Song H and Wang Z 2017 Hollow SnNi@PEO nanospheres as anode materials for lithium ion batteries *Int. J. Hydrogen Energy* 42 15290–8
- [7] Roy P and Srivastava S K 2015 Nanostructured anode materials for lithium ion batteries J. Mater. Chem. A 3 2454–84
- [8] Wang N, Ma X, Xu H, Chen L, Yue J, Niu F, Yang J and Qian Y 2014 Porous ZnMn<sub>2</sub>O<sub>4</sub> microspheres as a promising anode material for advanced lithium-ion batteries *Nano Energy* 6 193–9
- [9] Wang N, Xu H, Chen L, Gu X, Yang J and Qian Y 2014 A general approach for MFe<sub>2</sub>O<sub>4</sub> (M = Zn, Co, Ni) nanorods and their high performance as anode materials for lithium ion batteries J. Power Sources 247 163–9
- [10] Hou H, Tang X, Guo M, Shi Y, Dou P and Xu X 2014 Facile preparation of Sn hollow nanospheres anodes for lithium-ion batteries by galvanic replacement *Mater. Lett.* 128 408–11
- [11] Park M-G, Song J H, Sohn J-S, Lee C K and Park C-M 2014 Co-Sb intermetallic compounds and their disproportionated nanocomposites as high-performance anodes for rechargeable Li-ion batteries J. Mater. Chem. A 2 11391–9
- [12] Park M H, Cho Y, Kim K, Kim J, Liu M and Cho J 2011 Germanium nanotubes prepared by using the Kirkendall effect as anodes for high-rate lithium batteries *Angew. Chem.* 123 9821–4
- [13] Fan L, Li X, Yan B, Li X, Xiong D, Li D, Xu H, Zhang X and Sun X 2016 Amorphous SnO<sub>2</sub>/graphene aerogel nanocomposites harvesting superior anode performance for lithium energy storage Appl. Energy 175 529–35
- [14] Wang X, Meng Q, Wang Y, Liang H, Bai Z, Wang K, Lou X, Cai B and Yang L 2016 TiO<sub>2</sub> hierarchical hollow rnicrospheres with different size for application as anodes in high-performance lithium storage Appl. Energy 175 488-94
- [15] Xiong D, Li X, Shan H, Yan B, Li D, Langford C and Sun X 2016 Scalable synthesis of functionalized graphene as cathodes in Li-ion electrochemical energy storage devices Appl. Energy 175 512–21
- [16] Hou H, Cao X, Yang Y, Fang L, Pan C, Yang X, Song W and Ji X 2014 NiSb alloy hollow nanospheres as anode materials for rechargeable lithium ion batteries *Chem. Commun.* 50 8201–3
- [17] Tarascon J-M and Armand M 2001 Issues and challenges facing rechargeable lithium batteries *Nature* 414 359–67
- [18] Ramireddy T, Rahman M M, Xing T, Chen Y and Glushenkov A M 2014 Stable anode performance of an Sbcarbon nanocomposite in lithium-ion batteries and the effect of ball milling mode in the course of its preparation *J. Mater.* Chem. A 2 4282–91
- [19] Zhang L, Zhao X, Jiang X, Lv C and Cao G 2001 Study on the insertion behaviors of lithium-ions into CoFe<sub>3</sub>Sb<sub>12</sub> based electrodes J. Power Sources 94 92–6
- [20] Allcorn E and Manthiram A 2015 High-rate, high-density FeSb-TiC-C nanocomposite anodes for lithium-ion batteries J. Mater. Chem. A 3 3891–900
- [21] Mosby J M and Prieto A L 2008 Direct electrodeposition of Cu<sub>2</sub>Sb for lithium-ion battery anodes J. Am. Chem. Soc. 130 10656–61
- [22] Baggetto L, Allcorn E, Unocic R R, Manthiram A and Veith G M 2013 Mo<sub>3</sub>Sb<sub>7</sub> as a very fast anode material for lithium-ion and sodium-ion batteries *J. Mater. Chem.* A 1 11163 0
- [23] Villevieille C, Ionica-Bousquet C, Fraisse B, Zitoun D, Womes M, Jumas J-C and Monconduit L 2011 Comparative study of NiSb<sub>2</sub> and FeSb<sub>2</sub> as negative electrodes for Li-ion batteries Solid State Ionics 192 351–5
- [24] Kim H and Cho J 2008 Template synthesis of hollow Sb nanoparticles as a high-performance lithium battery anode material *Chem. Mater.* 20 1679–81

- [25] Yang R, Huang J, Zhao W, Lai W, Zhang X, Zheng J and Li X 2010 Bubble assisted synthesis of Sn-Sb-Cu alloy hollow nanostructures and their improved lithium storage properties J. Power Sources 195 6811–6
- [26] Hou H, Jing M, Yang Y, Zhu Y, Fang L, Song W, Pan C, Yang X and Ji X 2014 Sodium/lithium storage behavior of antimony hollow nanospheres for rechargeable batteries ACS Appl. Mater. Interfaces 6 16189–96
- [27] Park C M and Sohn H J 2007 Black phosphorus and its composite for lithium rechargeable batteries Adv. Mater. 19 2465–8
- [28] Alcántara R, Lavela P, Ortiz G F, Tirado J L, Stoyanova R, Zhecheva E and Merino C 2004 Nanodispersed iron, tin and antimony in vapour grown carbon fibres for lithium batteries: an EPR and electrochemical study *Carbon* 42 2153–61
- [29] Park C-M, Yoon S, Lee S-I, Kim J-H, Jung J-H and Sohn H-J 2007 High-rate capability and enhanced cyclability of antimony-based composites for lithium rechargeable batteries J. Electrochem. Soc. 154 A917–20
- [30] Dailly A, Ghanbaja J, Willmann P and Billaud D 2003 Lithium insertion into new graphite-antimony composites *Electrochim. Acta* 48 977–84
- [31] Dailly A, Ghanbaja J, Willmann P and Billaud D 2004 Synthesis, characterization and lithium electrochemical insertion into antimony-based graphite composites *J. Power Sources* 136 281–4
- [32] Hassoun J, Derrien G, Panero S and Scrosati B 2008 The role of the morphology in the response of Sb-C nanocomposite electrodes in lithium cells J. Power Sources 183 339-43
- [33] Chen W X, Lee J Y and Liu Z 2003 The nanocomposites of carbon nanotube with Sb and SnSb<sub>0.5</sub> as Li-ion battery anodes *Carbon* 41 959–66
- [34] Hou H, Jing M, Yang Y, Zhang Y, Zhu Y, Song W, Yang X and Ji X 2015 Sb porous hollow microspheres as advanced anode materials for sodium-ion batteries *J. Mater. Chem.* A 3 2971–7
- [35] Tian X, He W, Cui J, Zhang X, Zhou W, Yan S, Sun X, Han X, Han S and Yue Y 2010 Mesoporous zirconium phosphate from yeast biotemplate J. Colloid Interface Sci. 343 344–9
- [36] Lee B-S, Son S-B, Park K-M, Lee G, Oh K H, Lee S-H and Yu W-R 2012 Effect of pores in hollow carbon nanofibers on their negative electrode properties for a lithium rechargeable battery ACS Appl. Mater. Interfaces 4 6702–10
- [37] Ryu I, Choi J W, Cui Y and Nix W D 2011 Size-dependent fracture of Si nanowire battery anodes *J. Mech. Phys. Solids* 59 1717–30
- [38] Ge M, Rong J, Fang X and Zhou C 2012 Porous doped silicon nanowires for lithium ion battery anode with long cycle life *Nano Lett.* 12 2318–23
- [39] Ni D, Sun W, Wang Z, Bai Y, Lei H, Lai X and Sun K 2019 Heteroatom-doped mesoporous hollow carbon spheres for fast sodium storage with an ultralong cycle life Adv. Energy Mater. 19 190003601–10
- [40] Kruk M and Jaroniec M 2001 Gas adsorption characterization of ordered organic–inorganic nanocomposite materials *Chem. Mater.* 13 3169–83
- [41] Guo Y G, Hu J S and Wan L J 2008 Nanostructured materials for electrochemical energy conversion and storage devices Adv. Mater. 20 2878–87
- [42] Liu Y and Zhang X 2009 Effect of calcination temperature on the morphology and electrochemical properties of Co<sub>3</sub>O<sub>4</sub> for lithium-ion battery *Electrochim. Acta* 54 4180–5
- [43] Cao B, Liu H, Xu B, Lei Y, Chen X and Song H 2016 Mesoporous soft carbon as an anode material for sodium ion batteries with superior rate and cycling performance J. Mater. Chem. A 4 6472–8
- [44] Fan X, Jiang A, Dou P, Ma D and Xu X 2014 Threedimensional ultrathin Sn/polypyrrole nanosheet network as

- high performance lithium-ion battery anode RSC Adv. 4 52074–82
- [45] He M, Kravchyk K, Walter M and Kovalenko M V 2014 Monodisperse antimony nanocrystals for high-rate Li-ion and Na-ion battery anodes: nano versus bulk *Nano Lett.* 14 1255–62
- [46] Hou H, Yang Y, Zhu Y, Jing M, Pan C, Fang L, Song W, Yang X and Ji X 2014 An electrochemical study of Sb/ acetylene black composite as anode for sodium-ion batteries *Electrochim. Acta* 146 328–34
- [47] Zhu Y, Han X, Xu Y, Liu Y, Zheng S, Xu K, Hu L and Wang C 2013 Electrospun Sb/C fibers for a stable and fast sodium-ion battery anode ACS Nano 7 6378–86
- [48] Tang K, White R J, Mu X, Titirici M M, van Aken P A and Maier J 2012 Hollow carbon nanospheres with a high rate

- capability for lithium-based batteries *ChemSusChem* **5** 400–3
- [49] Shi L, Li H, Wang Z, Huang X and Chen L 2001 Nano-SnSb alloy deposited on MCMB as an anode material for lithium ion batteries *J. Mater. Chem.* 11 1502–5
- [50] Qin J, He C, Zhao N, Wang Z, Shi C, Liu E-Z and Li J 2014 Graphene networks anchored with Sn@ graphene as lithium ion battery anode ACS Nano 8 1728–38
- [51] Lv H, Qiu S, Lu G, Fu Y, Li X, Hu C and Liu J 2015 Nanostructured antimony/carbon composite fibers as anode material for lithium-ion battery *Electrochim. Acta* 151 214–21
- [52] Guo M, Meng W, Liu X, Wang G, Bai Z, Wang Z and Yang F 2018 Electrochemical performance and morphological evolution of hollow Sn microspheres Solid State Ionics 325 120–7